Quantum remnants of absorptive bistability in the attojoule regime

Joseph Kerckhoff,* Michael A. Armen, and Hideo Mabuchi
Edward L. Ginzton Laboratory, Stanford University, Stanford, California 94305, USA

Current approaches to high spatial-density, ultra-low power photonic switching utilize optical resonators with small mode-volume and high quality-factor to enhance the effective nonlinearity of bulk materials such as Si [1] or InGaAsP [2, 3]. Such resonators likewise play a crucial role in cavity QED research with single emitters such as quantum dots [4, 5] or diamond nv-centers [6, 7]. Whereas atomic and solid-state cavity QED experiments are routinely analyzed using quantum models, research aimed towards switching applications typically employs classical electromagnetic methods to model nanophotonic versions of the bistability and hysteresis phenomena that have dominated optical computer engineering since the 1970s [8]. Classical optical models are ultimately incompatible with the technological goal of low switching energy, however, as the characteristic scale of one attojoule corresponds to $\lesssim 10$ photons at near-infrared wavelengths. Here we present experimental data on attojoule optical bistability that clearly illustrate the significance of quantum-optical effects for switching-related nanophotonic device physics.

We utilize a gas-phase atom as the nonlinear medium in a Fabry-Perot optical resonator, but the methods we use to analyze quantum effects can be applied straightforwardly to solid-state systems (as in [4, 5]). We characterize the dynamic input-output properties of the atom-cavity system in a parameter regime that would be expected, on the basis of semiclassical mean-field theory [9], to exhibit absorptive bistability with a hysteresis loop suitable for attojoule optical switching. Theoretical studies have shown [10–12] that quantum fluctuations of the cavity field and atomic dipole should induce spontaneous switching between the low- and high-transmission states, and thus destroy true optical bistability, when the energy separation of the semiclassical attractors is brought down to attojoule scale (tens of photons) through the use of a small mode-volume and high quality-factor resonator (except in the good cavity limit [10], which is not relevant to nanophotonics). A previous experimental study [13] of single-atom cavity QED in a similar parameter regime clearly demonstrated the validity of quantum (as opposed to semiclassical) methods for predicting steady-state observables, but here we take an important step further by recording dynamic signals that reveal quantum 'remnants' of bistable behavior in the attojoule regime. Finding ways to functionalize such remnant behavior in the design of robust attojoule photonic switches is an outstanding challenge for quantum engineering.

The Maxwell-Bloch Equations (MBEs) represent a semiclassical mean-field approximation to the cavity QED master equation in the limit of weak coupling and large atom number [9, 14]; they have been used extensively in prior research on optical bistability with atomic ensembles as the intracavity nonlinear medium and are amenable to analysis using the tools of dynamical systems theory [12, 15, 16]. In single-atom cavity QED with strong coupling and strong driving fields, the MBEs retain some relevance as a projection of the quantum master equation onto the sub-manifold of semiclassical atom-field states [17] and numerical studies have shown [12] that solutions of the full quantum model often mimic those of the MBEs qualitatively.

The MBEs predict absorptive optical bistability for the parameters of our experiment, as shown in Fig. 1a. The vertical axis represents input drive amplitude (with units of 27pW per $(E/\kappa)^2$), and the solution curve passes through horizontal planar coordinates corresponding to the real and imaginary parts of the steady-state complex field amplitude(s). A characteristic 'S-curve' appears with two stable solutions and one unstable solution co-existing over a range of drive strengths. Using identical parameters, the steady-state solution of the quantum master equation can be determined for each value of the input drive strength. Contours of the corresponding Wigner functions (quasi-probability distributions over complex amplitudes of the intracavity field [18]) are displayed for several drive strengths in Fig. 1b. A double-peaked structure emerges in a range of E/κ similar to the bistable region of the MBEs (and recurs at higher drive strengths, but this is associated with a distinct bifurcation). The two peaks of the distribution may be associated with the low- and high-amplitude branches of the semiclassical bistability curve, but in the quantum model neither is truly stable. In any single experimental trial the cavity field (and thus the output power) will spontaneously switch between low and high states, as shown in the experimental data of Fig. 1c (see below). Such stochastic switching is a dramatic consequence of quantum fluctuations in the attojoule regime and clearly must be taken into account in the design of practical switching devices.

In our experiment, laser cooled ^{133}Cs atoms are dropped into a Fabry-Perot optical resonator (length 27μm, field decay rate $\kappa/2\pi = 9.3$MHz) supporting a circularly-polarized, 852nm TEM_{00} mode actively frequency-stabilized relative to an atomic cycling transition (with dipole decay rate $\gamma_\perp/2\pi = 2.6$MHz). As an atom falls through the cavity mode it experiences a position-dependent coupling rate g (maximum $g_0/2\pi$ =56.8MHz at the cavity anti-

*Electronic address: jkerc@stanford.edu

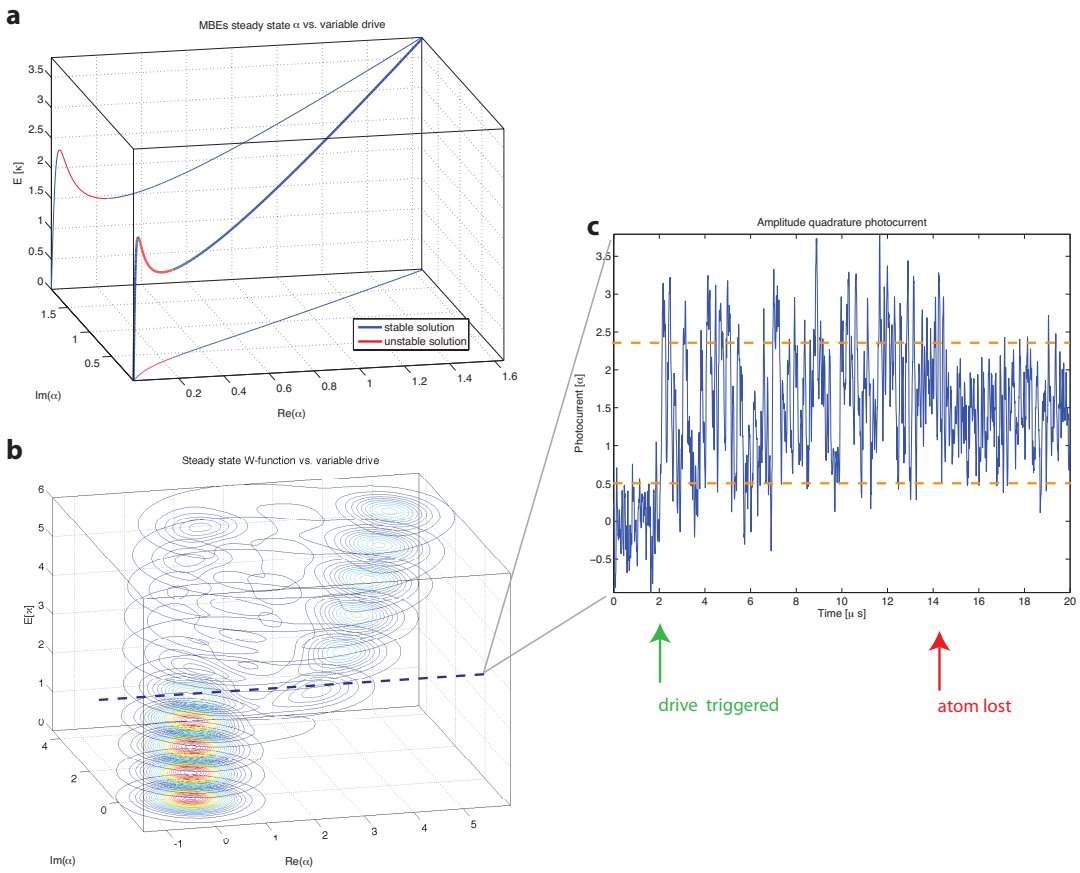

FIG. 1: **absorptive 'bistability' in single-atom cQED. a**, Steady state intra-cavity mode amplitude α from the semiclassical MBEs as a function of drive amplitude E for the experimental cQED system with $\{\Theta, \Delta\} = \{-1.1, .7\}\kappa$ mode-drive and atom-drive detunings. Blue (red) indicates dynamically stable (unstable) solutions, predicting true amplitude bistability for drives in the interval $E = [1.5, 2.3]\kappa$. The projection of the curve onto the bottom face of the coordinate box indicates the phases of the steady-state solutions, while the projection onto the back face illustrates the input-output relation for amplitude-quadrature homodyne detection. **b**, Wigner quasi-probability functions of the steady state cavity field from the quantum model as a function of drive amplitude for the same parameters as **a**. This quantum analysis predicts bimodal amplitude-quadrature field distributions merely evocative of the bistable, MBEs model. The reemergence of the low-amplitude state at the highest drives heralds the onset of dynamically distinct, dispersive 'bistability' behavior. **c**, Sample trace of amplitude quadrature homodyne measurement of the transmitted field during an atom transit. Upon detection of a maximally-coupled atom, a cw drive of $E = 2.6\kappa$ is turned on at 2μs, and rapid high-low amplitude switching (between levels indicated by dashed orange lines) is apparent until 14μs when the atom is abruptly lost and the measured transmission settles to a mid-amplitude, low-variance signal, indicative of an empty cavity. The gradual decrease in signal variance between 2 and 14μs is likely due to a gradual decrease in the coupling rate g from a initial, near-maximal value as the atom moves through the cavity mode.

nodes) that can be monitored via the transmission of a weak and detuned optical probe. Once a near-maximally coupled atom is detected, the probe power and detuning are adjusted for data acquisition (first arrow on the time axis in Fig. 1c, see appendix B). With the drive amplitude held at a fixed value within the bistable/bimodal region, the transmitted field is seen to switch stochastically between high and low states. Typically the atom-induced signal is lost after $\sim 10\mu$s, because the atom either exits the cavity mode or is pumped into a dark state, as signaled by the homodyne photocurrent settling to a mean and gaussian noise level indicative of transmission through an empty cavity (second arrow on the time axis in Fig. 1c).

In Fig. 2 we compare photocurrent distributions (histograms along the vertical axis of photocurrent segments such as the one between 'drive triggered' and 'atom lost' in Fig. 1c) obtained from experiments with three different sets of mode-drive, atom-drive detunings and drive amplitudes (Θ, Δ, and E, respectively). For a near-detuned system at the onset of 'bistability' with $\{\Theta, \Delta, E\} = \{-1.1, .7, 2.6\}\kappa$, wide/bimodal and narrow/normal distributions are apparent in the amplitude- and phase-quadrature distributions, respectively (Fig. 2d). However, when the atom-drive detuning is increased to $\Delta = 3\kappa$ for the same drive amplitude, the low-amplitude transmitted field dominates (Fig. 2e) as the drive threshold for 'bistability' increases with $|\Delta|$. The bimodal amplitude distribution reemerges when the

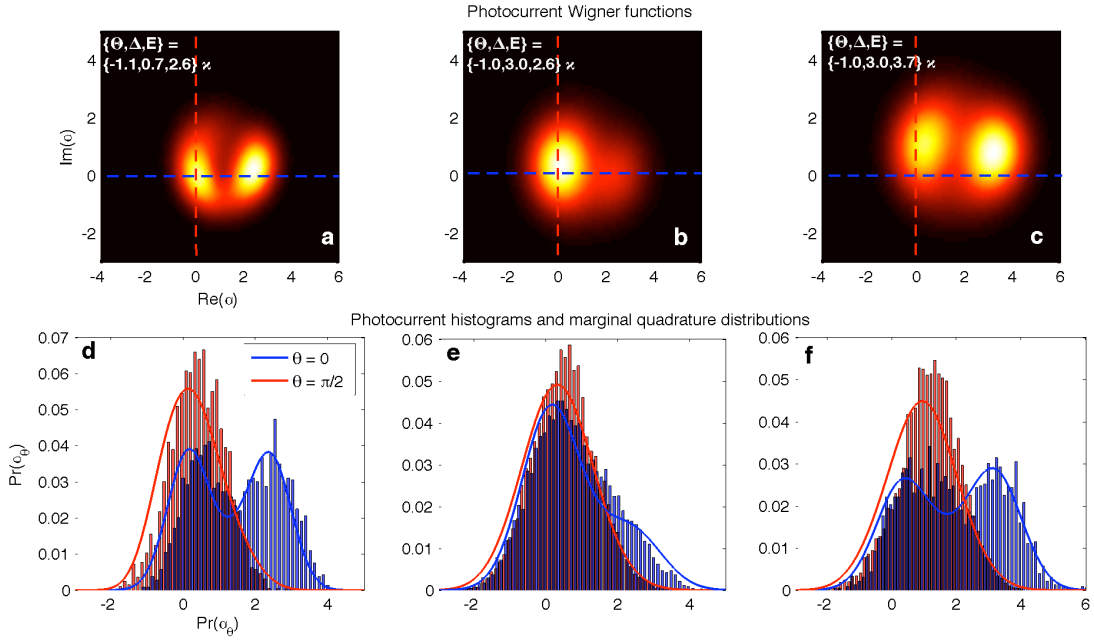

FIG. 2: **Steady state homodyne measurement distributions.** **a-c**, Wigner function-type representations of the expected steady state photocurrent distributions, using calibrated detection efficiencies and bandwidths. Marginal distributions of homodyne measurements of any quadrature may be obtained by integrating these representations over the complementary (perpendicular) quadrature (see appendix A). **d-f**, Histograms represent the phase- ($\alpha_{\pi/2}$) and amplitude-quadrature (α_0) photocurrent distributions from an ensemble of the highest-variance single-shot segments, presented at 20MHz detection bandwidth and overall cavity photon detection efficiency varying from 10% to 20% (due to free-space mode-matching drifts in the homodyne detector) for three sets of detuning and drive parameters. The histograms are compared with theoretically expected distributions obtained from corresponding Wigner functions (**a-c**, respectively). The only theoretically fit parameter assumes a static $g = .8 \times g_0$, approximating estimated distributions in g due to Zeeman sub-state distributions and atomic motion through the mode.

drive amplitude is increased to $E = 3.7\kappa$ in Fig. 2f. The data are in agreement with quantum theoretical predictions (using calibrated detection efficiency and bandwidth, see appendix A), despite the use of a somewhat idealized model that assumes a static coupling rate g (whereas g actually depends upon atomic position and Zeeman sub-state, and can vary within a photocurrent segment because of atomic motion and optical pumping). A fixed effective value $g = .8 \times g_0$ provides a good visual fit for all three parameter sets. We believe that this approximation of fixed g and the finite (20 MHz) bandwidth of our presented homodyne signals account for slight mismatches between theory and experiment of the amplitude quadrature splitting and phase-quadrature mean in the three data sets.

Hence, even in the attojoule regime, the distinct high- and low-amplitude states of the intracavity field are not washed out completely by quantum fluctuations. Remnant signatures of optical bistability are visible in the bimodal output photocurrents of Fig. 2 and also in a sort of 'kinetic' (as opposed to equilibrium) hysteresis that will be described below. We first establish from the photocurrent data that when an atom is present in the cavity, although the output field fluctuates strongly (switches spontaneously) it remains correlated over timescales much longer than that of light transmitted through an empty cavity (Fig. 3). This atom-induced memory effect can be seen as a quantum remnant of classical optical bistability, where classically the high- and low-amplitude states are truly stable and would therefore exhibit infinite correlation time. Consequently, it should still be possible to observe the hysteretic amplitude response characteristic of classical optical bistability by modulating the system drive slowly compared to the timescale for relaxation of the intracavity field (set in our case by the cavity decay time) but rapidly compared to the 'metastable' memory timescale indicated in Fig. 3. Accordingly, the data in Fig. 4 were obtained by recording amplitude-quadrature homodyne photocurrents while sweeping the drive strength sinusoidally at 0.25MHz or 1MHz. Figs. 4a and 4b depict representative single-shot photocurrent segments encompassing several cycles of sinusoidal drive amplitude modulation (AM) spanning the bimodal/bistable region. Increases in both the mean and variance of the output photocurrent, largely in phase with the drive amplitude, can be discerned in both of these real-time plots. However, plotting the photocurrent as a function of the instantaneous drive amplitude (Figs. 4c and 4d) reveals a significant hysteresis in the system response at 1MHz AM that is barely noticeable at .25MHz. Whereas the response

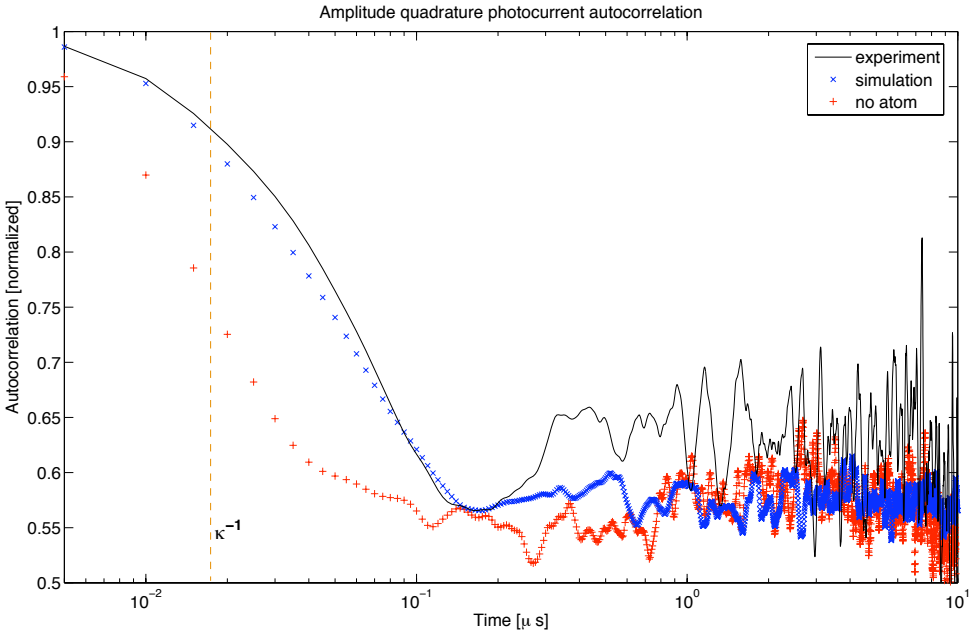

FIG. 3: **Steady state signal autocorrelation.** The autocorrelation function for the same amplitude quadrature photocurrent data presented as a histogram in figure 2d is displayed in black. Blue crosses represent the autocorrelation of photocurrents simulated by quantum trajectory methods (see appendix A) for identical parameters, but roughly 5 times longer aggregate duration. The autocorrelation of these quasi-bistable signals is clearly enhanced relative to experimental empty cavity transmission data (red pluses), also presented here with a 20MHz analog bandwidth, and the $\kappa^{-1} = 17$ns cavity decay time (dashed orange line) characterizing the intracavity field relaxation of the empty resonator. We attribute the elevated autocorrelation of the atom-cavity transmission data at long timescales to dynamic fluctuations in g, as in Fig 2.

of the empty cavity is linear and non-hysteretic with fixed (shot-noise limited) output photocurrent variance at these modulation frequencies, nonlinear increases in the signal mean and variance are evident in both traces at mid-sweep. At 1MHz AM, a hysteresis loop appears to open between the upward and downward drive amplitude sweeps, with the low (high) state persisting over a wider range of increasing (decreasing) drive amplitudes than at .25MHz AM. These data are in agreement with theoretical predictions assuming a fixed value of $g \approx .8 \times g_0$ (as was used for Fig. 2). We note that the slight elevation of the experimental high-amplitude branch in Fig. 4d is consistent with Fig. 2d.

While the quantum fluctuation-limited lifetimes of the low- and high-amplitude states in attojoule optical 'bistability' may be too short for direct use in photonic switching, our results clearly illustrate that existing theoretical models can be used to predict and analyze the dynamic response of real devices. Such models can be used to make detailed predictions of the impact of quantum effects on ultra-low energy switch performance, and should be adopted more widely by the photonic engineering community. Beyond mere simulation and analysis, existing theoretical methods can be used to explore new approaches to the suppression of quantum fluctuations in the design of switches and related nanophotonic devices, for example by exploiting embedded coherent feedback control [19, 20]. Even in a purely classical information processing paradigm, high spatial-density and ultra-low power nanophotonic circuit design presents intriguing new challenges for the nascent applied physics discipline of quantum engineering.

Acknowledgments

This work is supported by DARPA-MTO under Award No. FA8650-10-1-7007.

Appendix A: cQED modeling and photocurrent predictions

The driven Jaynes-Cummings Hamiltonian [21, 22] is a standard quantum model of the internal dynamics of a two-level atom coupled to an optical resonator mode in a frame rotating with the external drive ($\hbar = 1$)

$$H = \Delta\sigma^\dagger\sigma + \Theta a^\dagger a + ig(a^\dagger\sigma - a\sigma^\dagger) + iE(a^\dagger - a), \tag{A1}$$

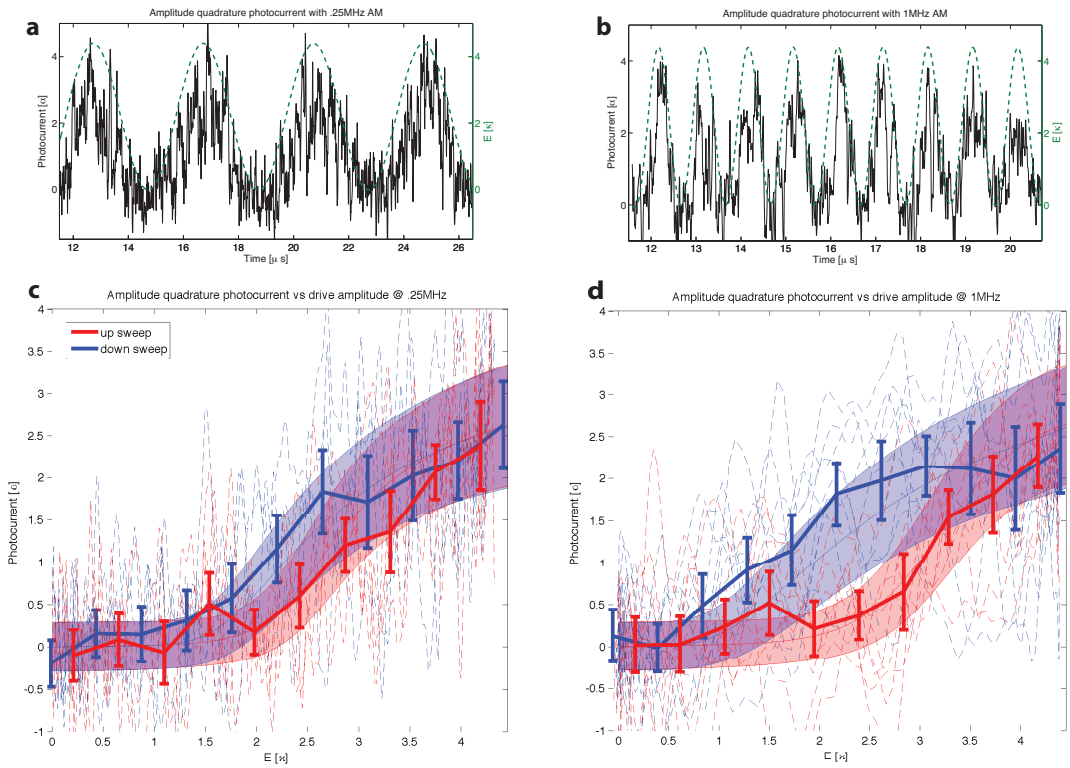

FIG. 4: **Amplitude hysteresis with fast modulation. a, b**) Single-shot, amplitude quadrature measurements of $\{\Theta, \Delta\} = \{-1.1, .7\}\kappa$ detuned systems with the drive amplitude swept at .25MHz and 1MHz, respectively. Black traces are 20MHz bandwidth photocurrents while the green, dashed traces represent the instantaneous drive amplitude. **c, d**) dashed red (blue) traces portray the same photocurrent data in **a** and **b**, respectively, as a function of the instantaneous, increasing (decreasing) drive amplitude. Error bars represent sample mean and variance of photocurrents within non-overlapping drive amplitude intervals. Red and blue regions represent theoretically expected photocurrent mean and sample variance as a function of instantaneous drive (see appendix A).

where a is the cavity mode annihilation operator, σ is the atomic lowering operator and † denotes the Hermitian conjugate. From left to right, the RHS terms correspond to the atom-drive detuning, the mode-drive detuning, the atom-mode coupling, and the external drive, respectively. The complete quantum model of this system comes from extending these Hamiltonian dynamics to include processes associated with the dissipation of photons through the cavity mirrors at mean rate 2κ per intra-cavity photon and excited atomic state spontaneous emission at mean rate $2\gamma_\perp$, as modeled by a and σ operator-coupling to external quantum fields [21, 23]. Only one of these fields, the transmitted mode, is monitored by our homodyne detection setup. For many applications, the entire model may be effectively represented by a *master equation* that describes the unconditional evolution of any mode and/or atom operator O (in the Heisenberg picture) [23, 24]

$$\frac{d}{dt}O \;=\; i[H,O] + 2\kappa\left(a^\dagger O a - \frac{1}{2}a^\dagger a O - \frac{1}{2}O a^\dagger a\right) + 2\gamma_\perp\left(\sigma^\dagger O \sigma - \frac{1}{2}\sigma^\dagger\sigma O - \frac{1}{2}O\sigma^\dagger\sigma\right) \equiv \mathcal{L}O. \tag{A2}$$

For example, the (one dimensional) null space of the analogous, Schrödinger picture 'Liouvillian,' $\mathcal{L}_S$, corresponds to the steady state density matrix utilized in Figs. 1b and 2 in the main Letter. This model may be trivially extended to describe the interaction of any number of two level atoms with the mode (or even with multiple modes).

Starting from this quantum model, the Maxwell-Bloch Equations (MBEs) may be derived by first assuming the approximation that atom-mode operator expectations factor [9, 12], *e.g.* $\langle a\sigma^\dagger\rangle \approx \langle a\rangle\langle\sigma^\dagger\rangle$ (see also [17]). This approximation is equivalent to modeling the cavity mode as if it were a noiseless classical field coupling to a two-level atom or to an ensemble of atoms (as the case may be). The MBEs can take the form of a set of five real, first-order, non-linear differential equations of motions for $\langle a\rangle$ and other expectations. Steady state solutions for $\langle a\rangle$ (proportional to the mean field transmitted by a Fabry-Perot cavity) and their dynamical stability may be found. Properly scaled, these mean-field solutions depend on the atom(s)-mode coupling only through a dimensionless parameter known as the 'cooperativity,' $C = Ng^2/2\kappa\gamma_\perp$, where N is the number of coupled atoms and g the rate of coupling to a single atom [12]. Thus, as long as the cooperativities are equal in both cases, this model predicts equivalent steady states for

a coupled atom and for a coupled macroscopic atomic ensemble. For highly non-linear, $C \gg 1$ systems, however, the correlations between discrete excitations in the mode (photons) and the atom(s) that are ignored in the mean-field model may play a significant role in the overall dynamics when $N \sim 1$, as demonstrated in the main Letter, with our experimental C=67, N=1 system.

Measurements of the external field transmitted by the cQED system are modeled using a quantum stochastic differential equation (QSDE) framework [24, 25]. Loosely speaking, this model represents observables of the transmitted field that are measured by our homodyne detection setup as a linear combination of cavity mode observables and quantum 'white noises.' For example, expected photocurrent distributions and correlations may be calculated from the characteristic functional [24, 25]

$$\Phi_T[\beta_s] = \langle \mathcal{T} \exp\left\{ \int_0^T \beta_s dB^\dagger_{out,s} - \int_0^T \beta^\dagger_s dB_{out,s} \right\} \rangle \tag{A3}$$

where β_s is some complex-valued scalar function of time, $B_{out,s}$ is the QSDE annihilation process of the measured, transmitted field, $\mathcal{T}$ is the time-ordering operator, and the expectation is taken over both the system and external field degrees of freedom.

Assuming a boxcar averaging photocurrent filter of width τ, the Fourier transform of equation (A3) produces a representation of the field analogous to a Wigner quasi-probability distribution

$$W_t(\alpha) = \frac{1}{\pi^2} \int d^2\alpha e^{\alpha\beta^\dagger - \alpha^\dagger\beta} \mathrm{Tr}\left[e^{\tau(\mathcal{L} - \frac{1}{2}|\beta|^2 + \mathcal{J})} \rho_t \right] \tag{A4}$$

where ρ_t is the reduced density matrix for the cQED system alone at time t (may be the steady state density matrix, for example), $\mathcal{J}\rho_t = \beta\sqrt{2\kappa\eta}\rho_t a^\dagger - \beta^\dagger\sqrt{2\kappa\eta} a\rho_t$, and η is the efficiency with which photons decaying from the cavity are measured by the homodyne detector. As with a Wigner function, $P_t(\alpha_\theta)$, the probability that a homodyne measurement of quadrature θ at time t will take the (real) value α_θ, is obtained by integrating $W_t(\alpha)$ over the axis in the (complex) α plane perpendicular to the axis at angle θ to the Re(α)-axis,

$$P_t(\alpha_\theta) = \int d\alpha_{\theta+\pi/2} W_t(\alpha). \tag{A5}$$

In practice, we approximate $W_t(\alpha)$ by assuming short photocurrent integration times so that we may 'freeze' the relevant internal dynamics over the sample interval, $\tau\mathcal{L} \to 0$, as done in Fig. 2 of the main Letter.

Similarly, integrating equation A3 over some $\beta_{\theta+\pi/2}$-quadrature produces the characteristic functional

$$\Phi_{\theta,T}[k] = \langle \exp\left\{ i \int_0^T k_s dY^\dagger_{\theta,s} \right\} \rangle, \tag{A6}$$

where $dY_{\theta,s}/dt \equiv I_s$ is the homodyne photocurrent operator of quadrature θ, which may be used to calculate moments of instantaneous photocurrent measurements [24, 25]

$$\langle I_{t_1} ... I_{t_n} \rangle = (-i)^n \frac{\partial^n}{\partial k_{t_1} ... \partial k_{t_n}} \Phi_{\theta,T}[k]|_{k=0}, \tag{A7}$$

which were used to calculate the expected experimental photocurrent sampling statistics in Fig. 4 of the main Letter, again using a $\mathcal{L}\tau \to 0$ approximation.

Finally, while we could have used Eqs. (A7) and (A2) to calculate the expected steady state autocorrelation of homodyne measurements in Fig. 3 of the main Letter, we instead relied on quantum trajectory methods [23], which compliment the above master equation-based approaches. While the master equation may be used to model ensembles of experimental realizations, a simulated quantum trajectory may be used to construct potential experimental homodyne measurement sequences, correctly sampled from the space of all possible sequences. For example, simulation of an amplitude quadrature photocurrent given a set of experimental parameters first involves the calculation of a possible trajectory for the internal quantum state vector $|\psi_c(t)\rangle$ by numerically integrating the stochastic Schrodinger equation [23, 26]

$$\begin{aligned} d|\psi_c(t)\rangle \;=\; & -(iH + \kappa a^\dagger a + \gamma_\perp \sigma^\dagger\sigma)|\psi_c(t)\rangle dt + \left(\sqrt{2\kappa}\langle a + a^\dagger\rangle_c dt + dW_t^{(1)}\right)\sqrt{2\kappa} a|\psi_c(t)\rangle + \\ & \left(\sqrt{2\gamma_\perp}\langle \sigma + \sigma^\dagger\rangle_c dt + dW_t^{(2)}\right)\sqrt{2\gamma_\perp}\sigma|\psi_c(t)\rangle \end{aligned} \tag{A8}$$

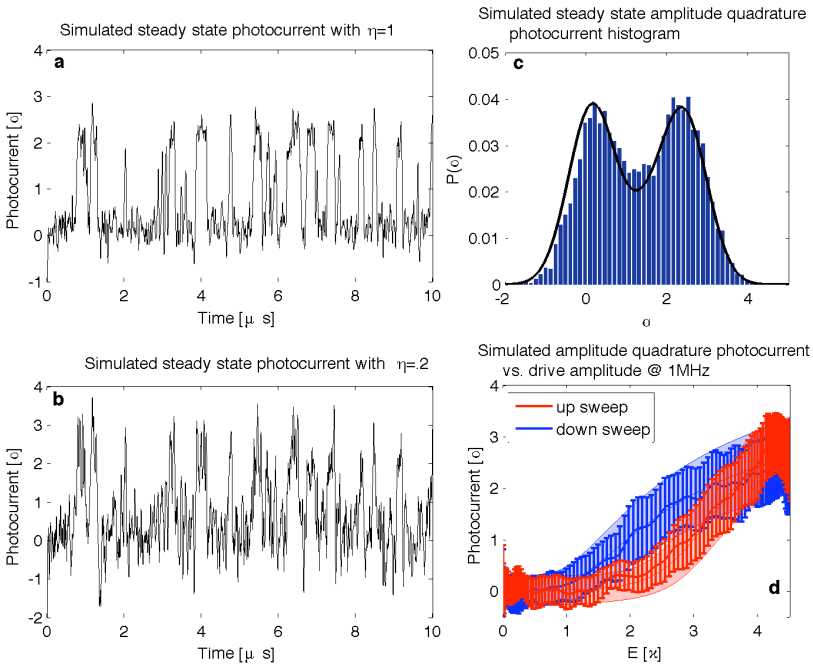

FIG. 5: **Simulated photocurrents.** Reproduction of several figures in the main Letter replacing experimental data with simulated photocurrent data produced by quantum trajectory methods. **a**, Simulated amplitude quadrature photocurrent data with $\{\Theta, \Delta, E\} = \{-1.1, .7, 2.6\}\kappa$, 20MHz analog bandwidth and perfect detection efficiency. **b**, Same quantum trajectory realization as **a**, but with the 20MHz bandwidth photocurrent simulated with $\eta = .2$ efficiency. **c**, Histogram of simulated inefficient photocurrents in comparison to the expected distribution derived from master equation based techniques. **d**, Sample mean and standard deviation of simulated photocurrents from fifty 1MHz AM cycles.

where $\{dW_t^{(1)}, dW_t^{(2)}\}$ are randomly generated, independent Wiener increments, $\langle\cdot\rangle_c$ denotes expectation w.r.t. $|\psi_c(t)\rangle$ and the state vector is forcibly re-normalized after each recursive update. The simulated photo-increment dY_t may then be obtained using this state trajectory and calibrated detection efficiency η by

$$dY_t = \sqrt{\eta}\left(\sqrt{2\kappa}\langle a + a^\dagger\rangle_c dt + dW_t^{(1)}\right) + \sqrt{1-\eta}dW_t^{(3)} \tag{A9}$$

where $dW_t^{(3)}$ is a third, independent Wiener increment. This method was used to create the simulated signal that was the basis of the simulated autocorrelation function in Fig. 3 of the main Letter.

Again, quantum trajectory simulations more directly reproduce time-series, experimental measurements, while master equation-based simulations represent ensembles of trajectories or measurements. In Fig. 5 we present many of the same figures in the main Letter using simulated photocurrent data based on quantum trajectories in comparison with the master equation predictions. Figs. 5a and b depict simulated amplitude quadrature photocurrents with the same experimental parameters as in Figs. 1c and 2d in the main Letter. In Fig. 5a, the measurement of the the mode leaking from the cavity is simulated as detected with perfect efficiency, while Fig. 5b simulates the same realization, but with our experimentally typical 20% efficiency. Fig. 5c histograms a simulated inefficient photocurrent trajectory in comparison with the expected amplitude quadrature distribution using equation (A4) (*i.e.* reproducing Fig. 2d in the main Letter using simulated data). Finally, Fig. 5d compares the sample mean and variance of simulated amplitude quadrature measurements during 50 cycles of a 1MHz AM external drive, for comparison to Fig. 4 in the main Letter. Both Figs. 5c and d utilize several times more aggregate data than the experimental data presented in the main Letter. As we expect both types of systems to be ergodic, we have empirically confirmed that the main discrepancies between quantum trajectory and master equation based simulations observed in Fig. 5 arise from the marginal appropriateness of the $\tau\mathcal{L} \to 0$ approximation when modeling 20MHz bandwidth signals derived from our system.

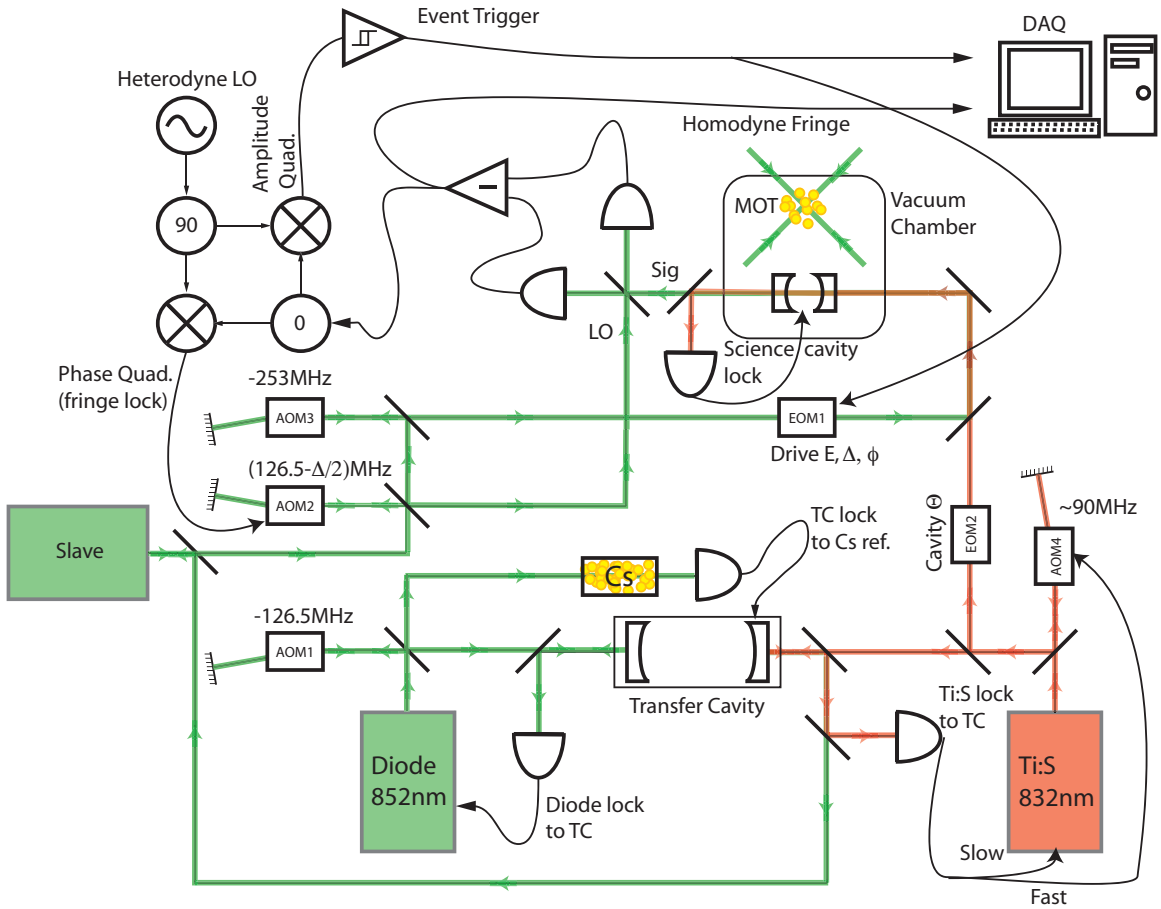

FIG. 6: **cQED stabilization, driving, and detection configuration.** The figure presents the essential optical and electro-optical components that define and stabilize the science cavity resonance frequency, drive the cQED system, detect individual atom transits, and perform homodyne detection of the cQED transmitted field, as explained in the text.

Appendix B: Experimental apparatus

The experiment consists of a standard cQED setup involving laser cooled ^{133}Cs atoms and a high finesse Fabry-Perot optical resonator [27, 28]. Through frequency and polarization selectivity, we attempt to drive only the $\left(6S_{1/2}, F=4, m_F=+4\right) \rightarrow \left(6P_{3/2}, F=5, m_F=+5\right)$ atomic cycling transition at 852nm in order to approximate the atom as a two-level system. Although the cavity used in the experiment was constructed to optimize signatures of dispersive 'bistability' at high drive amplitudes [29], it proved well-suited to study the amplitude 'bistabiliy' dynamics presented in the main Letter.

Inside a UHV ($\approx 10^{-9}$Torr) chamber and placed on a multi-stage vibration-isolation stack, the Fabry-Perot optical resonator is formed by two high-reflectivity (8ppm transmission, 2ppm loss), 10cm radii of curvature dielectric mirrors with roughly 27μm of separation, yielding a 300,000-finesse optical resonator for the standing wave, TEM$_{00}$, 18μm-waist transverse spacial mode with a field decay rate of $\kappa = 2\pi \times 9.3$MHz. We took particular care to mount the mirrors in a rotationally-symmetric manner to minimize stress-induced birefringence in the mirror coatings, allowing for full polarization-selectivity of the atomic transitions. The cavity length is tuned and actively stabilized by two shear-mode piezoelectric plates underlying the two mirror mounts. The precise cavity length and resonance frequency is continually stabilized by the Pound-Drever-Hall (PDH) [30] method using an additional laser probe detuned by the desired probe/cavity resonance frequency by two cavity free spectral ranges (at an optical wavelength of roughly 826nm, which interacts negligibly with Cs).

A Doppler-limited, magneto-optically trapped ensemble (MOT) of $\sim 10^6$ atoms is formed roughly 1cm above the cavity mode in the UHV chamber. After cooling, the ensemble trap is switched off, allowing the cold atoms to fall under gravity towards the cavity mode and by the time they reach the cavity mode their free-fall velocity tends to dominate any residual thermal motion. Due to the strong coupling between the targeted atomic transition and the

cavity mode (with calculated maximum value $g_0 = 2\pi \times 56.8$MHz at the cavity anti-nodes, using the dipole strength of the atomic transition and cavity mode volume), individual atom transits are detected by monitoring the (g-dependent) cavity transmission amplitude using a relatively weak and near-resonant probe, a free space balanced photodetector, and an actively phase-locked optical local oscillator (LO). Once a near-maximally coupled atom has been detected, the probe power and frequency shift to the desired experimental levels and data acquisition is initiated. Although multiple atom transits per drop may be visible, the atomic ensemble is sufficiently diffuse such that no more than one atom is simultaneously present in the cavity mode and we acquire data from only one transit per ensemble drop.

Fig. 6 depicts many aspects of the resonance lock, optical drive, transmission measurement, and atom-triggering in the experiment (the laser cooling optical system is standard and remains tacit). A diode laser is PDH frequency locked 253MHz to the blue of a large, mechanically stable 'transfer' cavity mode, which is itself locked 253MHz to the red of the $\left(6S_{1/2}, F=4\right) \rightarrow \left(6P_{3/2}F=5\right)$, 852nm hyperfine transition (so that the diode laser is on atomic resonance). The purpose of this $\sim 80,000$ finesse, 10kHz-linewidth transfer cavity is two-fold: provide a stable, Cs-locked frequency reference for all the lasers and act as a cleaning cavity for the diode laser, producing a more narrow linewidth 852nm laser source in transmission than is easily achievable in the laser lock. The 852nm beam transmitted by the transfer cavity seeds a high power slave laser, which sources the light used in both the science cavity drive and optical local oscillator. The 'drive' arm of the slave output is frequency shifted to the red of the atomic transition again before entering the first electro-optic modulator (EOM), which adds the optical carrier sideband near atomic resonance that serves as the science cavity's dynamic drive (the carrier and other sidebands are sufficiently detuned from the cQED system and have no measurable effect). The science cavity is actively stabilized by a second, titanium-sapphire laser at roughly 826nm and frequency locked relative to the 852nm diode laser via a lock to the transfer cavity. An optical sideband exactly two free spectral ranges to the red of the desired science cavity resonance near the atomic resonance, is defined by a second EOM and used to PDH resonance lock the science cavity in transmission.

For detecting and triggering off of near-maximally coupled atoms during the $\sim 50\mu$s time they make a full transit through the mode, the drive is initially tuned several MHz from the desired frequency for the experiment and its amplitude is set below the level of atomic saturation, while the several mW optical LO is tuned to the experimental drive frequency. Both heterodyne quadratures of the transmitted atom-probe are detected via their interference with the optical LO. The heterodyne phase quadrature is used to stabilize the relative phase of the free-space LO against slow drifts in the signal and LO path lengths via a 1kHz bandwidth optical phase lock loop. The amplitude quadrature is monitored by a Schmitt trigger that fires when the measured field amplitude drops below a threshold indicating a near-maximally coupled atom in the cavity. This trigger shifts the drive amplitude, frequency and LO-relative phase to the desired experimental configuration and initiates data acquisition of the homodyne photocurrent at 200MS/s. Although collected at full bandwidth, the data presented in the main Letter has been analog post-filtered at 20MHz for clarity.

---

[1] Yang, X., Husko, C., Wong, C. W., Yu, M. & Kwong, D.-L. Observation of femtojoule optical bistability involving Fano resonances in high-Q/Vm silicon photonic crystal nanocavities. *Appl. Phys. Lett.* **91**, 051113 (2007).

[2] Nozaki, K., *et al.* Sub-femtojoule all-optical switching using a photonic-crystal nanocavity. *Nature Photonics* **4**, 477-483 (2010).

[3] Kumar, R., *et al.* 10-GHz all-optical gate based on a III-V/SOI microdisk. *IEEE Photonics Technology Letters* **22**, 981-983 (2010).

[4] Srinivasan, K. & Painter, O. Linear and nonlinear optical spectroscopy of a strongly coupled microdisk-quantum dot system. *Nature* **450**, 862-865 (2007).

[5] Faraon, A., *et al.* Coherent generation of non-classical light on a chip via photon-induced tunnelling and blockade. *Nature Physics* **4**, 859-863 (2008).

[6] Barclay, P. E., Fu, K.-M. C., Santori, C. & Beausoleil, R. G. Chip-based microcavities coupled to nitrogen-vacancy centers in single crystal diamond. *Appl. Phys. Lett.* **95**, 191115 (2009).

[7] Englund, D., *et al.* Deterministic coupling of a single nitrogen vacancy center to a photonic crystal cavity. *Nano Lett.* **10**, 3922-3926 (2010).

[8] Smith, S. D. Optical bistability, photonic logic, and optical computation. *Appl. Opt.* **25**, 1550-1564 (1986).

[9] Lugiato, L. A. in *Progress in Optics*, edited by Wolf, E. (North-Holland, Amsterdam, 1984), Vol. XXI.

[10] Savage, C. & Carmichael, H. J. Single-atom optical bistability. *IEEE J. Quantum Electron.* **24**, 1495-1498 (1988).

[11] Kozlovskii, A. V. & Oraevskii, A. N. Removal of single-atom optical bistability by quantum fluctuations. *J. Exp. Theor. Phys.* **88**, 1095-1101 (1999).

[12] Armen, M. A. & Mabuchi, H. Low-lying bifurcations in cavity quantum electrodynamics. *Phys. Rev. A* **73**, 063801 (2006).

[13] Hood, C. J., Chapman, M. S., Lynn, T. W. & Kimble, H. J. Real-time cavity QED with single atoms. *Phys. Rev. Lett.* **80**, 4157-4160 (1998).

[14] Carmichael, H. J. in *Frontiers in Quantum Optics*, edited by Pike, E. R. & Sarkar, S. (Adam Hilger, Bristol, 1986).

[15] Gang, H., Ning, C. Z. & Haken, H. Codimension-two bifurcations in single-mode optical bistable systems. *Phys. Rev. A* **41**, 2702 (1990).

[16] Gang, H., Ning, C. Z. & Haken, H. Distribution of subcritical Hopf bifurcations and regular and chaotic attractors in optical bistable systems. *Phys. Rev. A* **41**, 3975 (1990).

[17] Mabuchi, H. Derivation of Maxwell-Bloch-type equations by projection of quantum models. *Phys. Rev. A* **78**, 015801 (2008).

[18] Walls, D. F. & Milburn, G. J. *Quantum Optics* (Springer-Verlag, Berlin, 2008).

[19] Mabuchi, H. Coherent feedback control with a dynamic compensator. *Phys. Rev. A* **78**, 032323 (2008).

[20] Kerckhoff, J., Nurdin, H. I., Pavlichin, D. S. & Mabuchi, H. Designing quantum memories with embedded control: photonic circuits for autonomous quantum error correction. *Phys. Rev. Lett.* **105**, 040502 (2010).

[21] Berman, P., Ed. *Cavity Quantum Electrodynamics* (San Diego: Academic Press, 1994).

[22] Jaynes, E. T. & Cummings, F. W. Comparison of quantum and semiclassical radiation theories with application to the beam maser. *Proc. IEEE* **51**, 89 (1963).

[23] Carmichael, H. *An Open Systems Approach to Quantum Optics* (Springer, Berlin, 1993).

[24] Gardiner, C. W. & Zoller, P. *Quantum Noise* (Springer-Verlag, Berlin, 2004).

[25] Barchielli, A. Direct and heterodyne detection and other applications of quantum stochastic calculus to quantum optics. *Quantum Opt.***2** 423-441 (1990).

[26] Tan, S. M. A computational toolbox for quantum and atomic optics. *J. Opt. B: Quantum Semiclass.* Opt. **1**, 424–432 (1999).

[27] Armen, M. A., Miller, A. E. & Mabuchi, H. Spontaneous dressed-state polarization in the strong driving regime of cavity QED. *Phys. Rev. Lett.* **103**, 173601 (2009).

[28] Mabuchi, H., Turchette, Q. A., Chapman, M. S. & Kimble, H. J. Real-time detection of individual atoms falling through a high-finesse optical cavity. *Opt. Lett.* **21**, 1393–1395 (1996).

[29] Kerckhoff, J., Armen, M. A., Pavlichin, D. S. & Mabuchi, H. The dressed atom as binary phase modulator: towards attojoule/edge optical phase-shift keying. `physics.optics/1011.1973` (2010).

[30] Drever, R. W. P. *et al.* Laser phase and frequency stabilization using an optical resonator. *Appl. Phys. B* **31** 97 (1983).